Dynamic genesis potential index for diagnosing present-day and future global tropical cyclone genesis

IOP Publishing Environ. Res. Lett. 15 (2020) 114008 https://doi.org/10.1088/1748-9326/abbb01

Environmental Research Letters

OPEN ACCESS

RECEIVED
22 July 2020

REVISED
9 September 2020

ACCEPTED FOR PUBLICATION
23 September 2020

PUBLISHED
16 October 2020

LETTER

Dynamic genesis potential index for diagnosing present-day and future global tropical cyclone genesis

Bin Wang[1,2] **and Hiroyuki Murakami**[3,4,5]

[1] Department of Atmospheric Sciences and International Pacific Research Center, The University of Hawaii at Manoa, Honolulu, HI, United States of America
[2] Earth System Modeling Center, Nanjing University of Science and Technology, Nanjing 210044, People's Republic of China
[3] University Corporation for Atmospheric Research, Boulder, CO, United States of America
[4] National Oceanic and Atmospheric Administration/Geophysical Fluid Dynamics Laboratory, Princeton, NJ, United States of America
[5] Meteorological Research Institute, Tsukuba, Ibaraki, Japan

E-mail: hir.murakami@gmail.com

Keywords: tropical cyclone, genesis potential index, climate change

Supplementary material for this article is available online

Abstract

Tropical cyclone (TC) genesis potential index (GPI) has been extensively used to understand the processes governing climate variability and future change of TC genesis (TCG). However, the relative roles of the thermodynamic versus dynamic environmental factors in TC genesis remain elusive, especially under a warming world. Here we show that four leading dynamic factors, the 850 hPa absolute vorticity, 500 hPa vertical motion, tropospheric vertical wind shear, and 500 hPa shear vorticity of zonal winds, are objectively identified by the logarithmic stepwise regression analysis from 11 dynamic and thermodynamic candidate factors. We further demonstrate that the model results from a TC-permitting global model ascertain the four leading dynamical factors as the most influential in both the present-day simulation and future projection under global warming. A dynamic GPI, consisting of the four dynamic parameters, provides a diagnostic tool for understanding future change of TC genesis. Meanwhile, it improves skills in representing interannual variations of TCG frequency in the western Pacific and Southern Hemisphere oceans.

1. Introduction

It has been widely recognized since Gray's (1968) pioneering work that tropical cyclone (TC) genesis requires constructive large-scale environmental conditions including sea surface temperature (SST), the planetary vorticity (latitude), the low-level relative humidity, and the magnitude of vertical wind shears. Gray (1979) developed the yearly genesis parameter (YP) that was able to replicate the main features of the seasonal and spatial variability of observed TC genesis. Several follow-up studies have devoted to improving the quantitative linkage between global TC genesis (TCG) number and environmental conditions (e.g. Royer *et al* 1998, Emanuel and Nolan 2004, Murakami and Wang 2010, Tang and Emanuel 2010, Tippett *et al* 2011).

The genesis potential index (GPI) has been widely used to diagnose interannual and interdecadal variability of TCG in North Atlantic Ocean (NA) (Gray 1979, Watterson *et al* 1995, Royer *et al* 1998, Goldenberg *et al* 2001) and to understand the processes by which El Niño-Southern Oscillation (ENSO) impact TCG globally (e.g. Camargo *et al* 2007). GPI values increase when large-scale conditions are favorable for TC genesis. The formulation for the GPI developed by Emanuel and Nolan (2004, ENGPI hereafter) is as follows:

$$ENGPI = (1.0 + 0.1 \times V_s)^{-2.0} \left(\frac{dRH_{600}}{50}\right)^3 \left(\frac{MPI}{70}\right)^3 \times \left|\zeta_{a850} \times 10^5\right|^{1.5} \quad (1)$$

where RH_{600} denotes the relative humidity (%) at 600 hPa; MPI represents the maximum potential intensity (m s^{-1}) which is an empirical value and is determined by the vertical structure of temperature and moisture and SST (Bister and Emanuel 1998); V_s is the magnitude of the vertical wind shear (m s^{-1}) between 200 and 850 hPa, and ζ_{a850} is the absolute vorticity (s^{-1}) at

850 hPa. The definition of MPI is based on Emanuel (1995), and modified by Bister and Emanuel (1998):

$$V_{\max}^2 = \frac{C_k}{C_D}\frac{T_s - T_o}{T_o}(h_o^* - h^*) \quad (2)$$

where C_k and C_D denote the surface enthalpy and momentum exchange coefficients; T_s is the sea surface temperature; T_o is the outflow temperature; h_o^* is the saturation moist static energy of the sea surface, and h^* is the saturation moist static energy of the free atmosphere.

Since the GPIs are derived from the climatological mean data, the extent to which the GPIs can explain interannual variability on the regional or basin-scale remains controversial (Waterson *et al* 1995). By comparing four TCG indices, i.e. ENGPI; the Gray (1979)'s Yearly Genesis Parameter; the Royer *et al* (1998)'s Modified Yearly Convective Genesis Potential Index; and the Tippett *et al* (2011)'s Index, Menkes *et al* (2012) found that all GPIs cannot reproduce interannual variations in the observed total TCG frequency, especially in the Indian Ocean and western North Pacific Ocean (WNP).

The large-scale factors controlling TC genesis may vary with time scales (Wang and Moon 2017). Using the ENGPI, Camargo *et al* (2009) found that vertical wind shear and MPI play a minor role, but the midlevel relative humidity makes the most significant contribution to the Madden–Julian Oscillation (MJO)-related genesis potential anomalies, followed by the low-level absolute vorticity. On the other hand, the 850 hPa relative vorticity weighted by the Coriolis parameter and 500 hPa vertical motion is found to be the most effective factors controlling intraseasonal TC genesis in both boreal winter and summer (Wang and Moon 2017, Moon *et al* 2018), suggesting a primary role of ambient circulation factors in modulating TCG on the intraseasonal time scale.

The GPIs have also been widely used to explain the physical processes behind the projected future changes of TCG (Yokoi and Takayabu 2009, Yamada *et al* 2010, Murakami and Wang 2010, Murakami *et al* 2011, Yokoi *et al* 2012). However, the relevance of the GPIs' thermodynamic factors in explaining TC changes under global warming has been challenged (Camargo *et al* 2014). The inconsistency between the TCG number and GPI in the projected future changes (Gualdi *et al* 2008); Yokoi and Takayabu 2009) may be because GPI is optimized for the present-day climate, in which MPI is a critical element. The MPI increases with rising sea surface temperatures (SSTs) and always projects a significant increase in genesis potential under global warming. However, the threshold SST value for TC genesis in a warming world will also increase (Wehner *et al* 2015, Sugi *et al* 2015), casting doubt on the applicability of the MPI-related GPI to understanding of future change of TCG. On the other hand, Murakami *et al* (2013) found that dynamic variables are of primary importance for separating developing and non-developing disturbances in the present-day climate in WNP, and such a relationship remains unchanged in a future warmer climate.

An improved understanding of the relationships between TCG and large-scale climate variables is of critical importance for predicting climate variation on various time scales and for understanding the projected future change of TCG. Our objective is to understand the relative roles of dynamic and thermodynamic factors that affect the TCG potential on the regional and global scales. Of particular interest is to explore the applicability of the GPI derived from the present-day climatology to the future projections in a warming world and to signify interannual variability of TCG in a basin or regional scale. With the gained knowledge and understanding, a new GPI is proposed and evaluated.

2. Datasets and methodology

2.1. Datasets

The observed TCG is determined from the IBTrACS (version v04r00; Knapp *et al* 2010) between 1979 and 2017. The IBTrACS consists of the TC data compiled by multiple organizations. In this study, we utilized the combination of the National Hurricane Center and the Joint Typhoon Warning Center. We consider only the TCs with tropical storm intensity (i.e. surface wind speeds of 35 kt) or above. TC genesis is considered when a storm intensity reaches 35 kt for the first time. All the genesis positions were counted for each grid box ($2.5° \times 2.5°$ or $5° \times 5°$) within the global domain, and the total count was defined as the TCG frequency. Observed SSTs over 1979–2017 were obtained from the UK Met Office Hadley Centre SST product (HadISST1.1; Rayner *et al* 2003). Five reanalysis datasets were used for the period 1980–2017: the NCEP/NCAR Reanalysis II (NCEP-2, Kanamitsu *et al* 2002); ECMWF Reanalysis Interim (ERA-Interim, Dee *et al* 2011); the Japanese 55-year reanalysis (JRA-55, Kobayashi *et al* 2015); NASA's The Modern-Era Retrospective analysis for Research and Applications, Version 2 (MERRA-2, Reichle *et al* 2017); and NCEP Climate Forecast System Reanalysis (CFSR, Saha *et al* 2010).

The dynamical model used in this study is the high-resolution, 20 km-mesh Meteorological Research Institute (MRI) Atmospheric General Circulation Model (AGCM) version 3.2 (MRI-AGCM3.2 S; Mizuta *et al* 2012, Murakami *et al* 2012). The MRI-AGCM3.2 S reasonably reproduces observed intense TCs of Category 4 and 5 and the global TC distribution (Murakami *et al* 2012). The successful simulations of TCs were mainly due to incorporating a new deep convection scheme (Yoshimura *et al* 2015), rather than the effect of high resolution (Murakami *et al* 2012). Two 25 yr experiments were conducted. The first is for the present-day period (1979–2003), and the second one is for the

future warmer climate state (2075–2099). The model simulation is forced by prescribing lower boundary conditions of SST and sea ice concentration (SIC). The observed monthly SST and SIC (HadISST1; Rayner *et al* 2003) are prescribed for the present-day experiment. The future projection is conducted with prescribed future SST, SIC, and atmospheric concentration of greenhouse gases (GHG), including CO_2 and aerosols, based on the Intergovernmental Panel on Climate Change (IPCC) Special Report on Emission Scenarios (SRES) A1B scenario (Solomon *et al* 2007). The A1B scenario assumes a future world of rapid economic growth, low population growth, and the rapid introduction of new and more efficient technologies, resulting in about 700 ppmv in CO_2 concentration at the end of this century. The future changes and trends of SST and SIC were estimated from the ensemble mean of 18 models from the World Climate Research Programme's Coupled Model Inter-comparison Project phase 3 [CMIP3; Meehl *et al* (2007)] under the IPCC A1B scenario.

2.2. Method for deriving the TC GPI

Assume Y and X_i represent the TCG potential index (GPI) and influential factors for TCG. We first calculate the correlation coefficients between log Y and log X_i using climatological monthly mean data. The stepwise regression and F-test are then used to select the significant top-ranking factors that make the best performing, multi-variable, linear-logarithmic regression equation:

$$\log(1+Y) = b + \sum_i a_i \log(X_i) \qquad (3)$$

where the subscript 'i' denotes the selected factors. Finally, we transform the linear-logarithmic equation to a nonlinear GPI by taking the logarithmic of both sides of the equation (3). The stepwise regression selects the influential factors in sequential order by maximizing the regressed fractional variance at each step (Jennrich and Sampson 1968). The Fisher's F-test was used to test the significance of the 'newly' added factor at each step based on its contribution to maximizing the increase of the regressed variance. This process continues until no statistically significant factors can be selected.

The climatological monthly mean data from January to December in the climatological TCG domains are used for both X_i and Y. The climatological TC domain was defined by all grids where the 39 yr (1979–2017) total TCG number exceeds some criteria N_c. Three resolutions were tested: 2.5° × 2.5°, 5° × 5°, and 10° × 10°. A 9-point smoothing was applied to the 2.5° × 2.5° and 5° × 5° grid cells to obtain smoothing distribution patterns. The smoothing conserves the total number of TCG. Sensitivity test indicates that $N_c = 1.5$, 5, and 20 provides optimal results for 2.5° × 2.5°, 5° × 5°, and 10° × 10° grid cells, respectively. The three optimal domains are similar for the three different grid sizes.

3. Objective selection of controlling factors for observed TC genesis

TCG locations are strongly constrained by the two factors recognized by Gray (1968), i.e. SST higher than 26.5 °C and the pre-TC vorticity seeding being sufficiently away from the equator so that Coriolis force can effectively spin up a TC (figure 1). These two factors can be considered as necessary conditions for TCG. As introduced in equation (1), Emanuel and Nolan (2004) used four influential factors to estimate the TCG potential: absolute vorticity at 850 hPa (ζ_a), relative humidity at 600 hPa (R), MPI (V_{pot}), and vertical wind shear between 200 and 850 hPa (V_s). In order to explore possible basin-dependence of the GPI, we consider seven more potential factors (table 1). All factors have a form of logarithm and their values range approximately from 0.4 to 2.7 when they are computed using the climatological monthly mean values. The adjustment of the logarithmic range acts as a normalization so that the ranges of variation are comparable for different candidate factors. The stepwise regression result is not sensitive to the range of logarithm.

Why do we implement the seven new factors? The absolute vorticity is a combination of two factors, and it is not clear which individual elements are region-dependent, so we test f and ζ_r, separately. The 500-hPa vertical pressure velocity (ω) is shown to be an important factor in NA (Murakami and Wang 2010) and TCG on the intraseasonal time scale (Wang and Moon 2017). The 500 hPa vorticity due to meridional shear of zonal winds (U_y) and the zonal wind convergence at 850 hPa (U_x) was suggested of importance in WNP and the zonal wind confluence zone (Fu. *et al* 2012, Peng *et al* 2012). Differing from the total vertical shear that depends only on the magnitude of the vertical shear, the vertical shear of zonal wind distinguishes the easterly and westerly vertical shear. From a dynamic standpoint, the easterly vertical shear, differing from the westerly vertical shear, favors for the development of low-level synoptic waves and TC (Wang and Xie 1996, Xie and Wang 1996) when its amplitude is not too large. The SST anomaly relative to the tropical (30°S–30°N) mean SST (SST_a) is selected over NA because previous studies have shown that the total number of TC genesis is substantially correlated with the relative SST anomalies in observations (e.g. Latif *et al* 2007, Swanson 2008, Vecchi *et al* 2008, Villarini *et al* 2010, Villarini and Vecchi 2012) and in dynamical models (Zhao *et al* 2010, Villarini and *et al* 2011, Ramsay and Sobel 2011, Murakami *et al* 2012, Knutson *et al* 2013).

The stepwise regression can objectively select factors in sequential order and determine an optimum combination of multi-factors. We measure

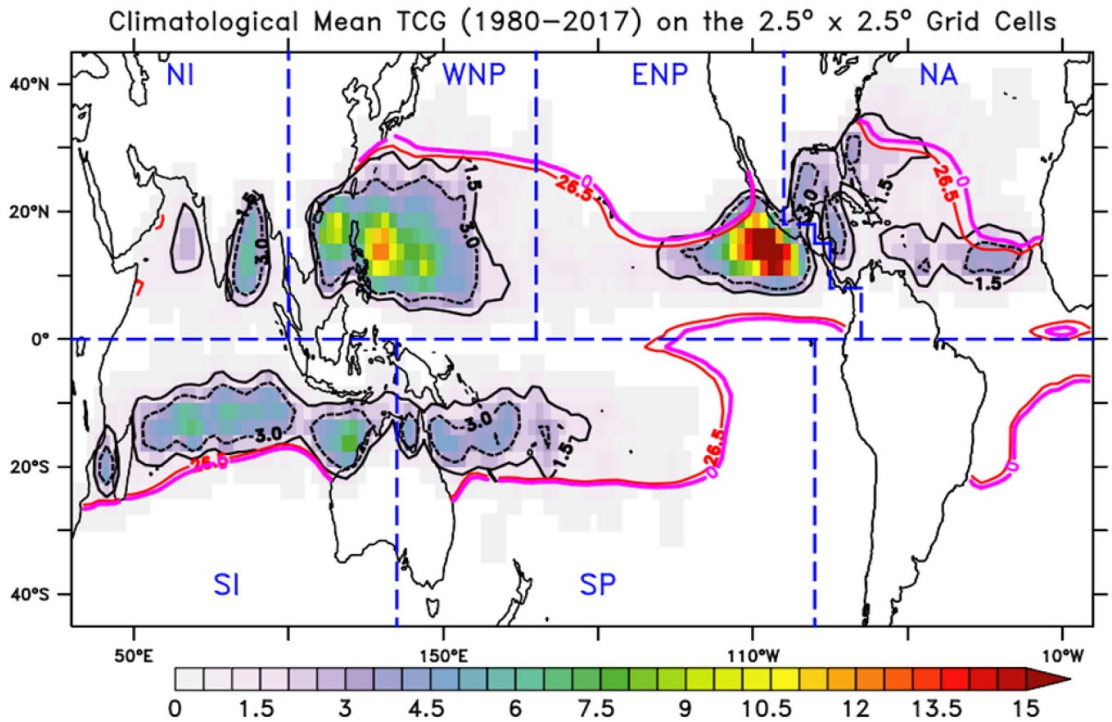

Figure 1. Climatological annual TC genesis frequency (TCG, number per year) at each 2.5° × 2.5° grid box derived from observations (1980–2017). A domain more than 1.5 (3.0) of TCG is shown in black solid (doted) lines. Red contour indicates 26.5 °C for the climatological mean SST derived from observations. Purple contour indicates the climatological mean SST or the zero line for the relative SST anomaly (SST_a). Blue texts denote the 6 ocean basins: North Indian Ocean (NI); western North Pacific Ocean (WNP); eastern North Pacific Ocean (ENP); North Atlantic Ocean (NA); South Indian Ocean (SI); and South Pacific Ocean (SP).

Table 1. List of the candidate predictors for establishing a new GPI. For each variable, equation (X_i) is used for deriving GPI formulation. Log Range indicates the minimum and maximum range of its logarithm value from monthly mean data using the ensemble mean reanalysis data. The Type indicates dynamical (Dyn) or thermodynamic (Thermo).

Symbol	Candidate variables	Description	Units	Range of logarithm
V_s	$2.0 + 0.1 \times \lvert ws_{200} - ws_{850} \rvert$	Vertical wind shear	$m.s^{-1}$	0.4–1.5
V_{zs}	$10 - 0.1 \times (u_{200} - u_{850})$	Zonal component of vertical wind shear	$m.s^{-1}$	1.5–2.7
ω	$5.0 - 20 \times \omega_{500}$	Vertical verocity at 500 hPa	$Pa.s^{-1}$	1.2–2.4
ζ_a	$5.5 + \lvert(\zeta_{850} + f) \times 10^5\rvert$	Absolute vorticity at 850 hPa	s^{-1}	0.5–2.0
f	$1.0 + \lvert f/f_0, f_0$ is f at 10°N	Coriolis parameter	-	0.4–1.4
ζ_r	$6.0 + \zeta_{850} \times 10^5$	Relative vorticity at 850 hPa	s^{-1}	1.0–2.0
U_y	$5.5 - \frac{\partial u_{500}}{\partial y} \times 10^5$	Meridional gradient of zonal wind at 500 hPa	s^{-1}	1.0–1.8
U_x	$5.0 - 2.0 \times \frac{\partial u_{850}}{\partial x} \times 10^5$	Zonal gradient of zonal wind at 850 hPa	s^{-1}	0.6–1.6
R	$2.0 + RH_{600}/7$	Relative humidity at 600 hPa	%	1.0–2.0
V_{pot}	$2.0 + mpi/20$	Maximum potential intensity	$m.s^{-1}$	0.8–2.0
SST_a	$9.0 + 0.5 \times (SST - \overline{SST}_{[30°S-30°N]})$	SST anomaly from tropical (30°S–30°N) mean	K	2.0–2.5

the relative importance of each candidate factor by the selected orders. Table 2 summarizes the commonality and difference in selected factors for the Northern Hemisphere (NH), Southern Hemisphere (SH), and global domains with five different reanalysis datasets and their ensemble mean. For the stepwise regression, we utilized the computational domain of $SST_a \geq 0$ because this domain, which is similar to SST $\geq$ 26.5 °C, represents the climatological TCG domain (figure 1). The ensemble mean reflects the majority of the five reanalysis results. Over the global domain, the first four selected factors are ζ_a, ω, V_s, and the meridional shear vorticity of the 500 hPa zonal winds (U_y). In the SH, the same four are selected, but the U_y was selected before V_s. In the NH, the first three are selected but U_y is replaced by the Coriolis parameter. The fourth factor reflects a hemispheric difference. As shown in figure 1, the SH TCG concentrates in a narrow latitudinal zone between 10°S and 20°S and from 50°E to 170°W along the Southern Indian Ocean and Southwest Pacific convergence zones where U_y is more relevant than earth's rotational effect. On the other hand, the NH TCG tends to cover a significantly larger latitudinal range, especially over WNP and NA, where the Coriolis parameter is important.

Table 2. Results of stepwise selection for the candidate variables. Stepwise regression is applied to the five individual reanalysis datasets and their ensemble mean dataset for the global (GL), Northern Hemisphere (NH), and Southern Hemisphere (SH) over the domain of $SST_a \geq 0$ (or SST $\geq$ 26.5 °C) on the 5° × 5° grid cells. Values shown are the complex correlation coefficients (CCCs). The superscript of the CCC indicates the order of the selection during stepwise regression.

	Reanalysis	V_s	V_{zs}	ω	ζ_a	f	ζ_r	U_y	U_x	R	V_{pot}	SST_a
GL	ERA-Interim	0.69^3		0.62^2	0.41^1	0.71^5		0.70^4				
	NCEP2	0.68^3		0.61^2	0.42^1	0.70^5		0.69^4				
	JRA55	0.69^3		0.63^2	0.41^1	0.71^5		0.70^4				
	MERRA2	0.43^1		0.69^3	0.62^2	0.71^5		0.70^4				
	CFSR	0.69^3	0.72^5	0.44^1	0.63^2			0.71^4				
	Enemble Mean	0.69^3		0.63^2	0.42^1	0.71^5		0.71^4				
NH	ERA-Interim	0.46^1		0.69^3	0.60^2	0.70^4						
	NCEP2	0.45^1		0.67^3	0.59^2						0.69^5	0.69^4
	JRA55	0.47^1		0.68^3	0.60^2	0.69^4						
	MERRA2	0.49^1		0.70^3	0.62^2	0.70^4						
	CFSR	0.50^1	0.72^4	0.70^3	0.59^2							0.72^5
	Enemble Mean	0.47^1		0.70^3	0.60^2	0.70^4						
SH	ERA-Interim	0.73^4		0.64^2	0.45^1		0.74^5	0.72^3				
	NCEP2	0.74^4		0.64^2	0.45^1		0.74^5	0.72^3				
	JRA55	0.74^4		0.66^2	0.45^1			0.73^3	0.74^5			
	MERRA2	0.73^4		0.63^2	0.45^1			0.70^3				0.73^5
	CFSR	0.74^4		0.63^2	0.46^1		0.75^5	0.72^3				
	Enemble Mean	0.74^4		0.65^2	0.46^1			0.72^3	0.75^5			

Results in table 3 explain how the four factors are selected for the global domain and why others not. Among the 11 parameters, three selected dynamic factors have the highest correlation coefficients (r) with the TCG frequency: ζ_a ($r = 0.42$), Vs ($r = -0.40$), and ω ($r = 0.39$). The fourth factor, U_y, is selected not because of its correlation with the observed TCG frequency but because it is complementary to all other three factors. Why are the thermodynamic factors, SST_a, R, and V_{pot}, not selected? The relative humidity, R, is highly correlated with ω ($r = 0.84$). This high correlation reflects a physical linkage between the two: 500 hPa ascent-related moisture convergence tends to moisten the lower troposphere and increase 600 hPa relative humidity. Thus, the role of R can be well represented by the 500 hPa vertical motion. The SST_a is significantly correlated with TCG frequency ($r = 0.33$), but it correlates even stronger with ω ($r = 0.65$) and V_s ($r = -0.51$); therefore, the stepwise regression considers it redundant after V_s and ω are selected. The MPI (V_{pot}) has an insignificant correlation with TCGF ($r = 0.25$) and highly correlated with SST_a ($r = 0.94$). Overall, the thermodynamic factors identified in earlier works are represented by the corresponding large-scale environmental dynamic factors once SST exceeds a critical value.

4. The GPI in a high-resolution GCM's present-day simulation and future projection

For the future projection of TCG, it is important to use those large-scale factors that are suitable for both the present-day climate and the future warming climate. For this purpose, we have conducted parallel analyses using the model outputs derived from the MRI 20 km-mesh, TC-permitting model (Murakami *et al* 2012) for the present-day simulation and future projection experiments. The large-scale climate variables and the model-resolved TCG numbers allow establishing the relationship between the TCG and GPI. Stepwise regressions are performed using the model outputs for each three different grid cells (2.5° × 2.5°, 5° × 5°, and 10° × 10°) and the global and each of six ocean basins. The selection score for each variable is defined as

$$\textit{The selection score} = \sum_{i}^{3}\sum_{j}^{7}\left(6 - x_{ij}\right) \qquad (4)$$

where i denotes each of three resolutions, j denotes each ocean basin, x_{ij} denotes the orders of the selected predictor for the ith resolution and jth ocean basin. Here we considered seven domains (the six ocean basins defined in figure 1 plus the global domain). The score is counted only when a variable is selected in the first five steps. A higher selection score indicates the variable tends to be selected in the earlier steps, representing its importance in the stepwise regression selection.

Figure 2 shows that the dynamical factors are consistently identified as the most influential factors in present-day simulation and future projection. For the present-day climate, V_s, ω, and ζ_a, are the most critical factors followed by f, ζ_r, V_{zs}, *and* U_y; while the thermodynamic factors are not prioritized (figure 2(a)). Thus, the model results derived from the present-day simulation are generally consistent with those obtained from the five reanalysis datasets. In the model's projected future warming climate, V_s, ω, and U_y are the most important factors followed by

Table 3. Mutual correlation coefficients among the 11 predictors and the predictand TCGF using the ensemble mean of the five reanalysis datasets within the domain of $SST_a \geq 0$ (or SST $\geq$ 26.5 °C) on the 5° × 5° grid cells. Numbers in bold highlight. Boldface font indicates a correlation coefficient with statistical significance at the 99% level by the student *t*-test.

	V_s	V_{zs}	ω	ζ_a	f	ζ_r	U_y	U_x	R	V_{pot}	SST_a
TCGF	**−0.40**	**0.27**	**0.39**	**0.42**	**0.35**	**0.26**	**0.16**	**0.14**	**0.30**	**0.25**	**0.33**
V_s		**−0.55**	**−0.36**	**0.08**	**0.17**	**−0.32**	**−0.31**	−0.01	**−0.43**	**−0.47**	**−0.51**
V_{zs}			**0.54**	**−0.26**	**−0.32**	**0.29**	**0.46**	**0.05**	**0.62**	**0.47**	**0.55**
ω				**−0.18**	**−0.25**	**0.33**	**0.39**	**0.24**	**0.84**	**0.63**	**0.65**
ζ_a					**0.96**	−0.00	**−0.36**	**0.07**	**−0.31**	**−0.24**	**−0.20**
f						**−0.26**	**−0.48**	**0.12**	**−0.39**	**−0.29**	**−0.25**
ζ_r							**0.51**	**−0.19**	**0.32**	**0.22**	**0.26**
U_y								−0.03	**0.46**	**0.38**	**0.35**
U_x									**0.06**	**0.24**	**0.26**
R										**0.56**	**0.57**
V_{pot}											**0.94**

f, ζ_a, and ζ_r (figure 2(b)). Again, the thermodynamic factors are not prioritized. The model simulation results indicate that the large-scale dynamical control of TC genesis tends to be stable from the present-day climate to the future global warming environment, suggesting that a set of dynamic controlling factors may be adequate for understanding the future change of the probability of TCG frequency under anthropogenically induced warming.

5. A new dynamic GPI for inferring global TC genesis

Using the four selected dynamic factors and the monthly climatological data on the 10° × 10° grids, we established the following approximate dynamic GPI (DGPI) formula:

$$DGPI = {V_s}^{-1} {U_y}^2 \omega^3 {\zeta_a}^2 e^{-12} - 1.0 \qquad (5)$$

where the terms of V_s, ζ_a, ω, and U_y are defined in table 1. In addition, we assume that TC genesis latitudes are 5 degrees away from the equator and SST is higher than 26 °C. Therefore, DGPI is set zero over the grids where SST < 26 °C or latitude within 5 degrees around the equator. Originally, stepwise regression yields the regression coefficients of −1.7, 2.3, 3.3, 2.4, and −11.8 for V_s, U_y, ω, ζ_a, and e, respectively. To build a simple form, we used lower rounded power values 2, 3, and 2 for the numerator factors U_y, ω, and ζ_a, and to balance the decreased powers in the numerators, we use −1 for the denominator factor V_s so that the DGPI computed by equation (5) is a good approximation. We have compared the DGPI in the exact form with the DGPI in the approximate form and found that the differences are not statistically significant.

To evaluate the diagnostic skill of the DGPI, we utilized the monthly mean large-scale variables derived from the ensemble mean of the five reanalysis datasets over a 2.5° × 2.5° grid box during the period from 1980 to 2017. Spatial correlation and root-mean-square error (RMSE) are computed for ENGPI and DGPI with reference to the observed TCG. Figure 3 shows that both GPIs can realistically capture the observed spatial patterns of TCG for the NH during May through October and for the SH during November through next April, although ENGPI moderately underestimates the maximum values over the North Pacific and South Indian Ocean (SI) (figure 3(b)).

The spatial distribution of TCG shows large year-to-year variability in association with ENSO. Camargo *et al* (2007) have shown that the ENSO-related TCG variability (the difference between the El Niño and La Niña years) diagnosed by ENGPI is in good agreement with observations. Similar to Camargo *et al* (2007), we computed the composite anomalies of DGPI for all El Niño years (figures 4(a)–(c)) and La Niña years (figures 4(d)–(f)), separately. Both ENGPI and DGPI display similar spatial anomaly patterns that are associated with ENSO compared with observations. DGPI shows a larger spatial contrast with a slightly higher spatial correlation than ENGPI during El Niño years. Results in figures 3 and 4 indicate that the DGPI and ENGPI have comparable skills in simulating climatology and the response of TCG to ENSO.

Figure 5 shows that the DGPI and ENGPI exhibit somewhat different strengths in diagnosing interannual variations of the basin-total GPI values over individual basins. Because the TC season starts in October and ends in April in the SH, use of the calendar year to count annual total TC number is inadequate. For this reason, we used the TC year, which starts in June and ends in next May, to describe year-to-year variability for both the NH and SH TCG (Wang *et al* 2010). Over the NA, both indices have the highest performance with spatial-correlation skills ($r = 0.77$), suggesting that the NA basin-scale TCG number can be best diagnosed by using large-scale environmental parameters. In the WNP, the interannual variability of TCG number is much better represented by DGPI ($r = 0.55$) variation than ENGPI ($r = -0.04$). In the eastern North Pacific Ocean (ENP), the ENGPI ($r = 0.63$) is better than the DGPI ($r = 0.37$). Over the SH, in both the South Pacific Ocean (SP) and

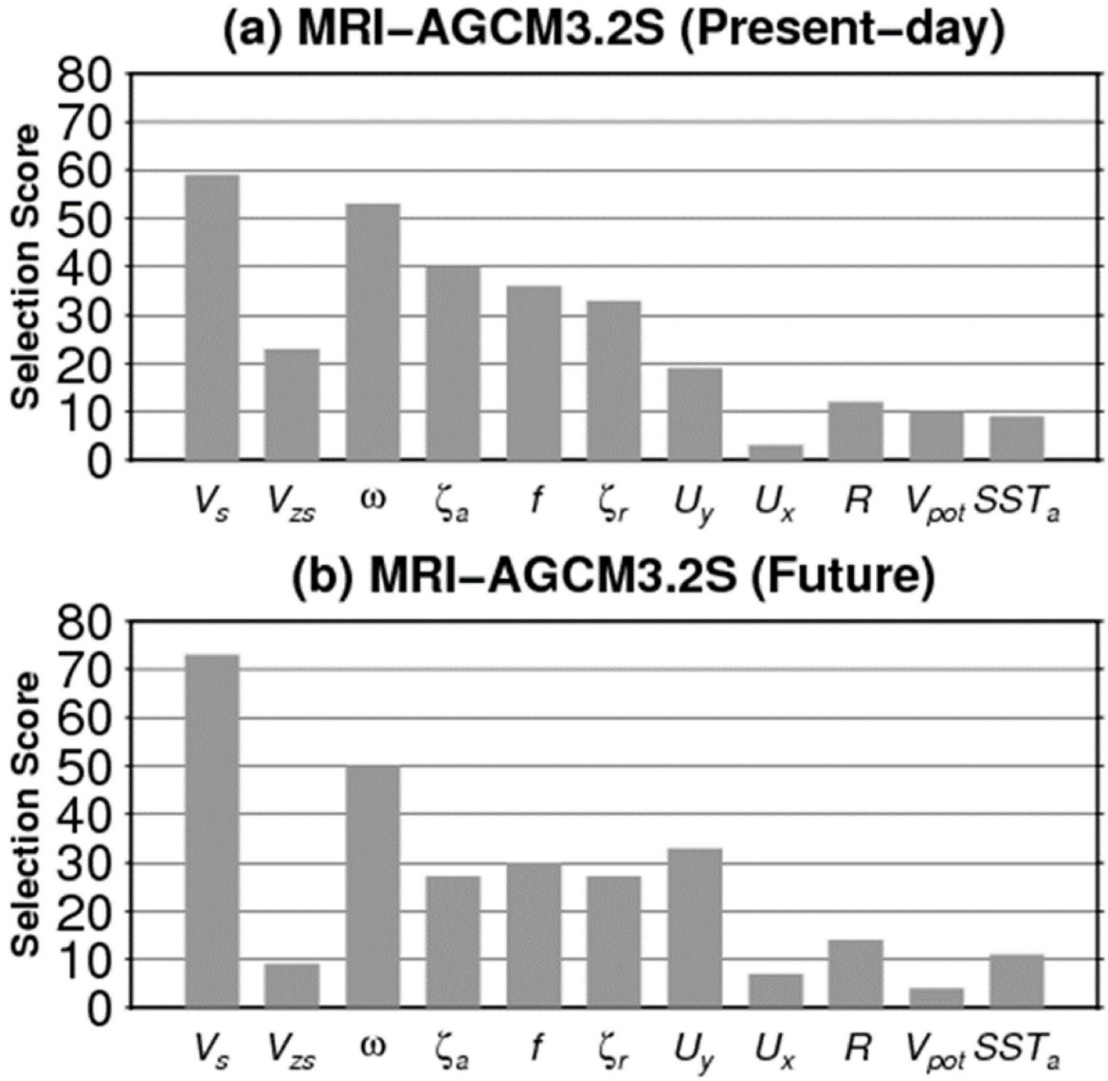

Figure 2. Summary of the most frequently selected variables in stepwise regression applied to the MRI 20-km-mesh AGCM for (a) the present-day (1979–2003) climate and (b) the projected future (2075–2099) climate. The selection score (defined as equation (4) in the main text) measures the importance of the variables in terms of the order of selection by the stepwise regressions. A high score indicates the variable tends to be selected in the earlier steps.

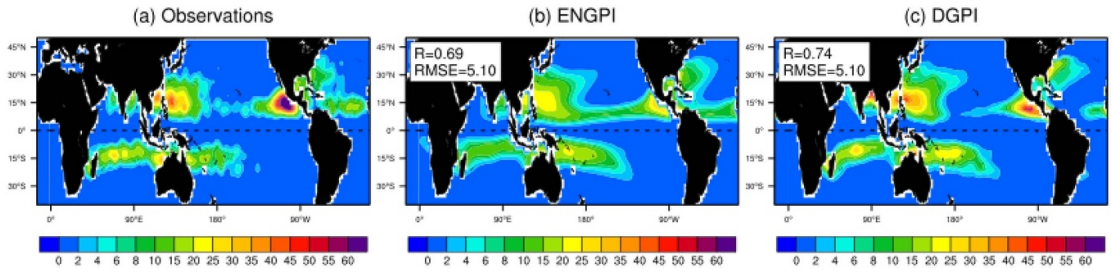

Figure 3. Comparison of observed (a) and diagnosed TCG numbers by using ENGPI (b) and DGPI(c). In NH shown are the climatological mean TCG number from May through October, while in the SH shown is the TCG number from November to the next April. GPI is applied to the ensemble mean of the five reanalysis datasets. Spatial correlation (R) and root-mean-square error (RMSE) are shown in the top left box of the corresponding panels for ENGPI and DGPI. The data covers the period of 1980–2017.

SI, the DGPI performs better than ENGPI. The main reason is that in the SH oceans, the 500-hPa U_y is the third leading factor for TCG (table 2). In the NI, both indices have the lowest skills, indicating that special effort should be made to represent the TCG variability during transitional monsoon seasons. Overall, the dynamic GPI shows significant skills in representing TCG variability in NA ($r = 0.77$), WNP ($r = 0.55$),

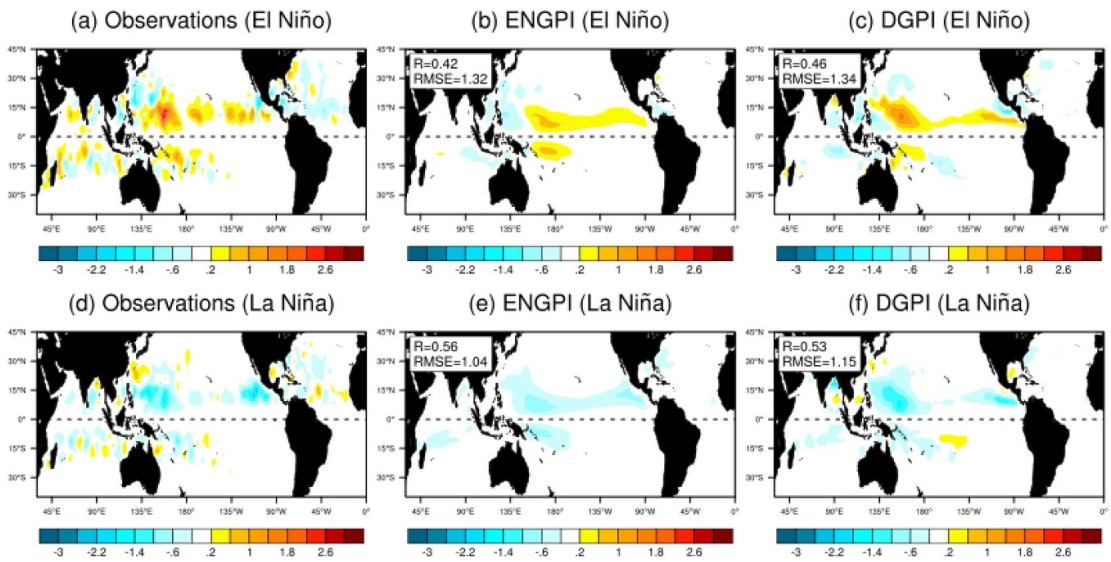

Figure 4. Same as in figure 3 except for comparison of observed (a) and diagnosed anomalous TCG numbers by using ENGPI (b) and DGPI(c) during El Niño (a)–(c) and La Niña years (d)–(f), respectively. The anomalous TCG number is obtained by compositing all El Niño and La Niña years, respectively, that have occurred during the period of 1980–2017.

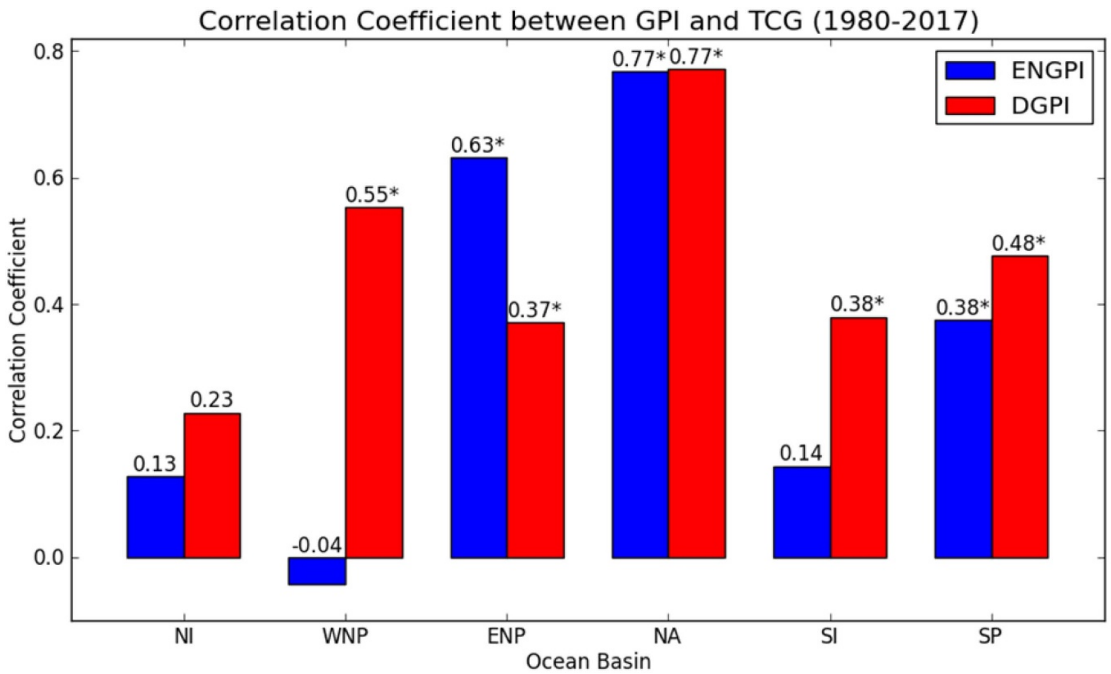

Figure 5. Correlation skills of the GPI in diagnosing the interannual variation of the basin total TCG. Shown are the correlation coefficients between the observed and diagnosed interannual variation of the basin total TCG number. Blue bars denote ENGPI, whereas red bars denote DGPI. The numbers over the bar indicate correlation coefficients. The asterisk indicates statistically significant at the 95% significance level using student *t*-test. The data period is 1980–2017. The ocean basins are defined in figure 1.

SP ($r = 0.48$), SI ($r = 0.38$), and ENP ($r = 0.37$). These correlations are statistically significant at the 95% confidence level.

6. Conclusion and discussion

We applied logarithmic stepwise regression with *F*-test to objectively assess the relative prominence of 11 large-scale environmental dynamic and thermodynamic factors that are potentially conducive to TCG in the global ocean and regional ocean basins. The most prominent factors selected for the global ocean by using five different reanalysis datasets are the 850 hPa absolute vorticity ζ_a, 500 hPa vertical velocity ω, and vertical wind shear V_s. The 500 hPa meridional shear of zonal winds U_y is the fourth factor for the global ocean and third in the SH oceans (table 2). The thermodynamic factors (i.e. the 600 hPa relative

humidity; SST_a; and maximum potential intensity) are highly correlated with and well represented by the dynamic factors (e.g. ω or V_s) (table 3).

A new dynamic genesis potential index (DGPI) for recognition of TCG potential in global oceans is established by using ζ_a, ω, V_s, and U_y. The DGPI and ENGPI have comparable ability to portray climatological mean distribution and the relationship between TCG and ENSO (figures 3, 4). For representing the year-to-year variations of basin total GPI numbers, the DGPI is better than ENGPI in the WNP, SP, and the South and North Indian Ocean (SI, NI), comparable over NA, but less skillful in the ENP (figure 5).

We demonstrate, using the MRI TC-permitting GCM experiments, that the four dynamical controlling factors are stable and selected for both the present climate and the future warming world (figure 2), suggesting that DGPI can be used to understand the causes of TCG changes under global warming.

A cautious note is that while the thermodynamic factors are not selected, it does not mean they are physically unimportant. The dynamic control of TCG implies that the dynamic factors can well represent the influence of these thermodynamic factors. More importantly, the dynamic factors are shown suitable for both the present-day climate and the future climate under significant global warming. The thermodynamic factors that are derived from the present-day climate, on the other hand, might not be fully applicable to the future climate as they may be sensitive to the effects of sea surface warming.

Several issues deserve further investigation. First, the selected factors show some basin-dependent features, but the first three dynamic factors, ζ_a, ω, and V_s (or its zonal component V_{zs}) remain the most common pickups (supplementary table S1 (available online at https://stacks.iop.org/ERL/15/114008/mmedia)). The differences are seen in some complementary factors selected, including the SST_a in the WNP and NA, U_y in the Southern Oceans, and R in the North Pacific. We have applied the stepwise regression to each basin and built basin-dependent GPIs, which show better skills in some ocean basins (e.g. WNP and SP) but not uniformly. In the vast ocean basins, one may consider deriving suitable GPI for some sub-regions. For instance, in the southeast quadrant of the WNP (0–17°N, 140–180°E), the correlation coefficient between a regional GPI and the total number of TCG can reach 0.80. Special effort should be placed on the Indian Ocean, where the current GPIs have poor skills in representing the interannual variability of TCG.

Another issue is whether the GPIs derived from climatology can faithfully reflect the interannual-to-multidecadal variability of TCG. To improve the capability of DGPI in representing the variability of the TCG number and better to elaborate the processes leading to the variability, we speculate that the derivation of DGPI by incorporating information of the interannual variability may be required. The additional information may help identify different large-scale factors responsible for the interannual variations of TCG from basin to basin.

While the dynamic GPI was shown to apply to a future warming scenario, the relative roles of the thermodynamic versus dynamic factors in TC genesis under a warning world remain unknown. This issue will be addressed in an accompanying work that compares the DGPI's and ENGPI's projected future changes of TC genesis potential against the TC-permitting models' projected TC genesis frequency.

Acknowledgments

BW is supported by the National Science Foundation (Climate Dynamics Division) Award No. AGS-1540783 and the National Natural Science Foundation of China (Grant No. 91437218). This paper is the IPRC publication #1475, and ESMC publication #324.

Data availability statement

The data that support the findings of this study are available upon reasonable request from the authors.

ORCID iDs

Bin Wang https://orcid.org/0000-0002-5726-108X
Hiroyuki Murakami https://orcid.org/0000-0002-1816-3452

References

Bister M and Emanuel K A 1998 Dissipative heating and hurricane intensity *Meteor. Atmos. Phys.* **52** 233–40
Camargo S J, Emanuel K A and Sobel A H 2007 Use of a genesis potential index to diagnose ENSO effects on tropical cyclone genesis *J. Climate* **20** 4819–34
Camargo S J, Tippett M K, Sobel A H, Vecchi G A and Zhao M 2014 Testing the performance of tropical cyclone genesis indices in future climates using the HiRAM model *J. Climate* **27** 9171–96
Camargo S J, Wheeler M C and Sobel A H 2009 Diagnosis of the MJO modulation of tropical cyclogenesis using an empirical index *J. Atmos. Sci.* **66** 3061–74
Dee D P *et al* 2011 The ERA-interim re-analysis: configuration and performance of the data assimilation system *Q. J. R. Meteorol. Soc.* **137** 553–97
Emanuel K A 1995 Sensitivity of tropical cyclones to surface exchange coefficients and a revised steady-state model incorporating eye dynamics *J. Atmos. Sci.* **52** 3969–76
Emanuel K A and Nolan D S 2004 Tropical cyclone activity and global climate *Proc. of 26th Conf. on Hurricanes and Tropical Meteorology* (American Meteorological Society, Miami, FL), pp 240–1
Fu B, Peng M S and Li T 2012 Developing versus nondeveloping disturbances for tropical cyclone formation. Part II: western North Pacific *Mon. Wea. Rev.* **140** 1067–80
Goldenberg B, Landsea C W, Mestas-Nuñez A M and Gray W M 2001 The recent increase in Atlantic hurricane activity: causes and implications *Science* **293** 474–9

Gray W M 1968 Global view of the origin of tropical disturbances and storms *Mon. Wea. Rev.* **96** 669–700
Gray W M 1979 Hurricanes: their formation, structure and likely role in the tropical circulation *Meteorology over the Tropical Oceans*, ed D B Shaw (Reading: Royal Meteorological Society) pp 155–218
Gualdi S, Scoccimarro E, Navarra A 2008 Changes in Tropical Cyclone Activity due to Global Warming: Results from a High-Resolution Coupled General Circulation Model. **21** 5204–5228
Jennrich M I and Sampson P F 1968 Application of stepwise regression to non-linear estimation *Technometrics* **10** 63–72
Kanamitsu M, Ebisuzaki W, Woollen J, Yang S-K, Hnilo J J, Fiorino M and Potter G L 2002 NCEP-DOE AMIP-II Reanalysis (R-2) *Bull. Amer. Meteor. Soc.* **83** 1631–43
Knapp K R, Kruk M C, Levinson D H, Diamond H J and Neuman C J 2010 The international best track archive for climate stewardship (IBTrACS): unifying tropical cyclone best track data *Bull. Amer. Meteor. Soc.* **91** 363–76
Knutson T R, Sirutis J J, Vecchi G A, Garner S, Zhao M, Kim H-S, Bender M, Tuleya R E, Held I M and Villarini G 2013 Dynamical downscaling projections of twenty-first-century Atlantic hurricane activity: CMIP3 and CMIP5 model-based scenarios *J. Climate* **26** 6591–617
Kobayashi S *et al* 2015 The JRA-55 reanalysis: general specifications and basic characteristics *J. Meteor. Soc. Japan* **93** 5–48
Latif M, Keenlyside N and Bader J 2007 Tropical sea surface temperature, vertical wind shear, and hurricane development *Geophys. Res. Lett.* **34** L01710
Meehl G A, Covey C, Delworth T, Latif M, Mcavaney B, Mitchell J F B, Stouffer R J and Taylor K E 2007 The WCRP CMIP3 multimodel dataset: A new era in climate change research *Bull. Amer. Meteor. Soc.* **88** 1383–94
Menkes C E *et al* 2012 Comparison of tropical cyclogenesis indices on seasonal to interannual timescales *Clim. Dyn.* **38** 301–21
Mizuta R *et al* 2012 Climate simulations using MRI-AGCM3.2 with 20-km grid *J. Meteor. Soc. Japan* **90A** 233–58
Moon J-Y, Wang B, Lee S S and Ha K-J 2018 An intraseasonal genesis potential index for tropical cyclones during Northern Hemisphere summer *J. Climate* **31** 9055–71
Murakami H *et al* 2012 Future changes in tropical cyclone activity projected by the new high-resolution MRI-AGCM *J. Climate* **25** 3237–60
Murakami H, Li T and Peng M 2013 Changes to environmental parameters that control tropical cyclone genesis under global warming *Geophys. Res. Lett.* **40** 2265–70
Murakami H and Wang B 2010 Future change of North Atlantic tropical cyclone tracks: projection by a 20-km-mesh global atmospheric model *J. Climate* **23** 2699–721
Murakami H, Wang B and Kitoh A 2011 Future change of western North Pacific typhoons: projections by a 20-km-mesh global atmospheric model *J. Climate* **24** 1154–69
Peng M S, Fu B and Li T 2012 Developing versus nondeveloping disturbances for tropical cyclone formation. Part I; North Atlantic *Mon. Wea. Rev.* **140** 1047–66
Ramsay H A and Sobel A H 2011 Effects of relative and absolute sea surface temperature on tropical cyclone potential intensity using a single-column model *J. Climate* **24** 183–93
Rayner N A, Parker D E, Horton E B, Folland C K, Alexander L V and Rowell D P 2003 Global analysis of sea surface temperature, sea ice, and night marine air temperature since the late nineteenth century *J. Geophys. Res.* **108** 4407
Reichle R, Liu Q, Koster R, Draper C, Mahanama S and Partyka G 2017 Land surface precipitation in MERRA-2 *J. Climate* **30** 1643–64
Royer J-F, Chauvin F, Timbal B, Araspin P and Grimal D 1998 A GCM study of the impact of greenhouse gas increase on the frequency of occurrence of tropical cyclones *Clim. Change* **38** 307–43
Saha S *et al* 2010 The NCEP climate forecast system reanalysis *Bull. Amer. Meteor. Soc.* **91** 1015–57
Solomon S, Qin D, Manning M, Marquis M, Averyt K, Tignor M M B, Miller H L Jr. and Chen Z (eds) 2007 *Climate Change 2007: The Physical Science Basis* (Cambridge: Cambridge University Press) pp 996pp
Sugi M, Yoshida K and Murakami H 2015 More tropical cyclones in a cooler climate *Geophys. Res. Lett.* **42** 6780–4
Swanson K L 2008 Nonlocality of Atlantic tropical cyclone intensities *Geochem. Geophys. Geosyst.* **9** Q04V01
Tang B and Emanuel K 2010 Midlevel ventilation's constraint on tropical cyclone intensity *J. Atmos. Sci.* **67** 1817–30
Tippett M K, Camargo S J and Sobel A 2011 A poisson regression index for tropical cyclone genesis and the role of large-scale vorticity in genesis *J. Climate* **24** 2335–57
Vecchi G A, Swanson K L and Soden B J 2008 Whither hurricane activity? *Science* **322** 687
Villarini G and Vecchi G A 2012 North Atlantic power dissipation index (PDI) and accumulated cyclone energy (ACE): statistical modelling and sensitivity to sea surface temperature *J. Climate* **25** 625–37
Villarini G, Vecchi G A, Knutson T R, Zhao M and Smith J A 2011 North Atlantic tropical storm frequency response to anthropogenic forcing: projections and sources of uncertainty *J. Climate* **24** 3224–38
Villarini G, Vecchi G A and Smith J A 2010 Modeling of the dependence of tropical storm counts in the North Atlantic basin on climate indices *Mon. Wea. Rev.* **138** 2681–705
Wang B and Moon J Y 2017 An anomalous genesis potential index for MJO modulation of tropical cyclones *J. Climate* **30** 4021–35
Wang B and Xie X 1996 Low-frequency equatorial waves in vertically shear flow. Part I: stable waves *J. Atmos. Sci.* **53** 449–67
Wang B, Yang Y, Ding Q, Murakami H and Huang F 2010 Climate control of the global tropical storm days (1965–2008) *Geophys. Res. Lett.* **37** L07704
Watterson I G, Evans J L and Ryan B F 1995 Seasonal and interannual variability of tropical cyclogenesis: diagnostics from large-scale fields *J. Climate* **8** 3052–66
Wehner M P, Reed K A, Stone D, Collins W D and Bacmeister J 2015 Resolution dependence of future tropical cyclone projections of CAM5.1 in the U.S. CLIVAR hurricane working group idealized configurations *J. Climate* **28** 3905–25
Xie X and Wang B 1996 Low-frequency equatorial waves in vertically sheared zonal flows. Part II: unstable waves *J. Atmos. Sci.* **53** 3589–605
Yamada Y, Oouchi K, Satoh M, Tomita H and Yanase W 2010 Projection of changes in tropical cyclone activity and cloud height due to greenhouse warming: global cloud-system-resolving approach *Geophys. Res. Lett.* **37** L07709
Yokoi S, Takahashi C, Yasunaga K and Shirooka R 2012 Multi-model projection of tropical cyclone genesis frequency over the Western North Pacific: CMIP5 results *SOLA* **8** 137–40
Yokoi S and Takayabu Y N 2009 Multi-model projection of global warming impact on tropical cyclone genesis frequency over the western North Pacific *J. Meteor. Soc. Japan* **87** 525–38
Yoshimura H, Mizuta R and Murakami H 2015 A spectral cumulus parameterization scheme interpolating between two convective updrafts with semi-Lagrangian calculation of transport by compensatory subsidence *Mon. Wea. Rev.* **143** 597–621
Zhao M, Held I M and Vecchi G A 2010 Forecasts of the hurricane season using a global atmospheric model assuming persistence of SST anomalies *Mon. Wea. Rev.* **138** 3858–68